PyTOAST: Python Top Of Atmosphere Simulation Tool

Document version 3.0: August 2023: PyTOAST v9

Contributing authors: Amir Ibrahim, Sean Bailey, Emerson Sirk, Andy Sayer, Lachlan McKinna, Fred Patt, Bryan Franz, and Jeremy Werdell

Introduction

PyTOAST generates simulated top-of-atmosphere Level-1B files for the PACE Ocean Color Instrument (OCI). PyTOAST utilizes retrieved surface and atmospheric properties and top-of-atmosphere (TOA) radiances from MODIS and VIIRS, pre-computed radiative-transfer look-up tables for the OCI spectral response, and spectral libraries of land and clouds to produce realistic radiometry in the standard Level-1B format (https://oceancolor.gsfc.nasa.gov/data/pace/format/) of OCI. The PyTOAST simulator is computationally efficient, and thus allows for large scale production of multi-day global data distributions with realistic viewing geometries for testing of retrieval software mechanics and data flow.

Theoretical Background

Clear sky over the ocean model

The simulator is based on a radiative coupling of various components of the atmosphere, ocean, and land surfaces as an inverse process to the atmospheric correction (Mobley et al., 2016). For a clear ocean pixel, the top-of-atmosphere (TOA) reflectance is calculated as follows:

$$\rho_t(\lambda; Geom) = \left(\rho_{path}(\lambda; Geom) + \rho_w'(\lambda; Geom) + \rho_{surface}'(\lambda; Geom) \right) \times T_g(\lambda; Geom). \,(1)$$

The TOA reflectance is a function of $Geom$ (i.e. solar zenith; θ_0, sensor zenith θ, and relative azimuth φ), and wavelength, λ; $\rho_{path}(\lambda; Geom)$ is the path reflectance due to scattering and absorption by air molecules (Rayleigh scattering) and aerosols; $\rho_w'(\lambda; Geom)$ is the ocean body reflectance, and $\rho_{surface}'(\lambda; Geom)$ is the reflectance contribution from surface glint and whitecaps, where both $\rho_w'(\lambda; Geom)$ and $\rho_{surface}'(\lambda; Geom)$ are expressed at the TOA after propagation through the atmosphere. $T_g(\lambda; Geom)$ is the two-way absorbing gas transmittance along the solar and sensor zenith. In the following sections we will briefly discuss each of the above terms.

Path reflectance:

The path reflectance is a summation of two terms, the Rayleigh reflectance and the aerosol reflectance including the aerosol-Rayleigh interaction:

$$\rho_{path}(\lambda; Geom) = \rho_r(\lambda; Geom) + \rho_a(\lambda; Geom). \,(2)$$

The $\rho_r(\lambda; Geom)$ term is calculated through the tabulation of vector radiative transfer (VRT) simulations. The Rayleigh optical depth, which is input to the VRT code, is calculated from Bodhaine et al. (1999). Although the path reflectance term is shown in Eqs. (1) and (2) as a function of only wavelengths and geometry, the Rayleigh reflectance is also a function of atmospheric surface pressure and surface windspeed, where the surface roughness model is based on the Cox-Munk windspeed to wave slopes relationship and the effect of pressure variation is modeled from Wang (1995).

The second term in Eq. (2) is the aerosol reflectance, which is calculated through the VRT code for 80 different aerosol models from Ahmad et al. (2010), where the microphysical properties of the aerosol models are calculated for a pre-determined set of 8 near-surface atmospheric relative humidities and 10 fine-mode volume fractions, and the aerosol vertical profile in the atmosphere is based on the Shettle and Fenn model (Shettle and Fenn 1979). The aerosol reflectance calculations include effects of multiple scattering and molecule-aerosol interaction within the atmosphere. The molecule-aerosol diffuse transmittance along the solar and sensor directions, $t_{sol}(\lambda, Geom)$ and $t_{sen}(\lambda, Geom)$, respectively, is also calculated and tabulated from the VRT simulations, and used to propagate the water and surface reflectance to the TOA.

To increase the speed of the aerosol reflectance computations, the Principal Component Analysis (PCA) method was used to reduce the dimension of the aerosol LUTs for each aerosol model. The dimension reduction using PCA brings the size of the LUT from 286 different bands to 30 principal components, significantly reducing the size of the LUTs and the processing time for each pixel. The number of principal components was chosen so that the reconstructed reflectances have errors well below the measurement uncertainty of OCI (i.e., <<0.5%). The aerosol reflectance is first standardized by subtracting the mean and dividing by the standard deviation of the data samples. The covariance matrix of the dataset is then calculated, and an eigen decomposition is performed to calculate the eigenvectors or the principal components. These principal components, along with the mean and standard deviation vectors, are stored in the LUTs rather than storing the direct reflectances. Thus, for each pixel, the LUT interpolation over the geometry and optical depth is performed over the principal component dimension rather than the larger wavelength dimension. After the interpolation step, the principal components are then converted to the wavelength dimension by applying the inverse PCA.

Ocean reflectance:

$\rho'_w(\lambda; Geom)$ is the ocean reflectance at TOA. The bottom of atmosphere (BOA) ocean reflectance $\rho_w(\lambda; Geom)$ is calculated through a forward model that provides the ocean reflectance as a function of chlorophyll-a (Chl-a; mg m^{-3}) concentration, $Geom$ and spectral inherent optical properties (IOPs; absorption and scattering coefficients). The BOA reflectance contribution is attenuated by the diffuse transmittance of the atmosphere, such that $\rho'_w(\lambda; Geom) = t_{sen}(\lambda, Geom) \times \rho_w(\lambda; Geom)$. The BOA ocean reflectances are generated from an ocean reflectance model (ORM) that derives the above-water remote sensing reflectance, $R_{rs}(\lambda;$ sr$^{-1})$, which is converted from nadir geometry to the desired solar and sensor path geometries using the bidirectional reflectance distribution function (f_{brdf}) of Morel et al. 2002, and then propagated to the TOA as:

$$\rho'_w(\lambda; Geom) = \pi R_{rs} t_{sol} t_{sen} / f_{brdf}. \text{ (3)}$$

In PyTOAST, $R_{rs}(\lambda)$ is derived using the ocean reflectance model (ORM) of the Generalized Inherent Optical Property algorithm framework (GIOP) (Werdell et al. 2013). The default configuration of the GIOP is currently used to derive OB.DAAC's distributed IOP data products[1]. Thus, by taking GIOP-derived level-3 IOP data products and returning them to the GIOP ORM forward model, one can closely approximate the original $R_{rs}(\lambda)$ observed by the ocean color sensor (e.g. MODIS, VIIRS) as well as simulate $R_{rs}(\lambda)$ at bands of other sensors such as OCI.

The GIOP ORM uses the quasi-single scattering approximation (QSSA) of (Gordon et al. 1988) that models the spectral remote sensing reflectance just below the air-ocean interface, $r_{rs}(\lambda)$, as a function of the total absorption ($a(\lambda)$; m^{-1}) and backscattering coefficients ($b_b(\lambda)$; m^{-1}):

$$r_{rs}(\lambda, 0^-) = 0.0949u(\lambda) + 0.0794u(\lambda)^2, \text{ (4)}$$

where,

$$u(\lambda) = \frac{b_b(\lambda)}{b_b(\lambda) + a(\lambda)} \text{ (5)}$$

The spectral coefficients $a(\lambda)$ and $b_b(\lambda)$ are additive terms and expressed as:

$$a(\lambda) = a_w(\lambda) + M_\phi a_\phi^*(\lambda) + M_{dg} a_{dg}^*(\lambda) \text{ , and (6)}$$

$$b_b(\lambda) = b_{bw}(\lambda) + M_p b_{bp}^*(\lambda) \text{ , (7)}$$

where w represents water, ϕ represents phytoplankton, dg represents colored dissolved and detrital matter, and p represents particulate matter. The terms with superscript asterix (*) represents normalized spectral coefficients with values of 1.0 at 443 nm. The M_ϕ, M_{dg}, and M_p terms are scalar magnitudes coefficients and represent $a_\phi(443)$, $a_{dg}(443)$, and $b_{bp}(443)$, respectively.

We treat both the absorption coefficient of water, $a_w(\lambda$; m^{-1}), and the backscattering coefficient of water, b_{bw} $a_w(\lambda$; m^{-1}), as spectral constants (Pope and Fry 1997; Zhang et al. 2009). The spectral shape for the absorption coefficient of colored dissolved and detrital matter, $a_{dg}^*(\lambda)$, was modelled using an exponential model of the form:

$$a_{dg}^*(\lambda) = e^{-0.018(\lambda-443)} \text{ (8)}.$$

The spectral shape of the particulate backscattering coefficient was modelled as:

$$b_{bp}^*(\lambda) = \left(\frac{443}{\lambda}\right)^\gamma \text{ (9)},$$

---

where the power law exponent, γ, is defined per Lee et al. (2002).

The spectral shape of the absorption coefficient of phytoplankton in the visible domain, $a*_{\phi,VIS}(\lambda)$, is modelled following (Bricaud et al. 1998). First, $a_{\phi}(\lambda)$ is modelled as a function of Chl-a and two spectral constants $A(\lambda)$ and $B(\lambda)$:

$$a_{\phi,VIS}(\lambda) = A(\lambda)\ [\text{Chl-a}]^{B(\lambda)-1}. (10)$$

Then, $a*_{\phi,VIS}(\lambda)$ is then computed as:

$$a^*_{\phi,VIS}(\lambda) = a_{\phi,VIS}(\lambda)/a_{\phi,VIS}(443). (11)$$

One limitation of the Bricaud et al. (1998) bio-optical model is that the spans only the visible spectral range (400 – 700 nm). For OCI simulated data, we wish to span the range (300 – 900 nm). To address this, we used 153 $a_{\phi}(\lambda)$ previously extracted from NASA's SeaBASS archive that range 250 – 800 nm (McKinna and Werdell 2019) to extend $a_{\phi}(\lambda)$ into the UV and NIR range. In the NIR, all 153 spectra were normalized to 1.0 at 700nm and an exponentially decaying function was fit through the data. From this analysis, the following model was determined for the spectral shape of phytoplankton in the NIR:

$$a^*_{\phi,NIR}(\lambda) = 55.123\lambda^{-0.0789} \ \text{ (when } \lambda > 700 \text{ nm). (12)}$$

For the UV domain (300 – 400 nm), the 153 $a_{\phi}(\lambda)$ spectra were normalized to 1.0 at 400 nm and then spectrally averaged. The result, $a*_{\phi,UV}(\lambda)$, was then smoothed with a gaussian kernel filter to remove residual noise/artifacts. The $a*_{\phi,UV}(\lambda)$ data are recorded in Table 2. We recognize that $a_{\phi}(\lambda)$ exhibits notable variability in the UV (e.g., see Figure 5 in Bricaud et al. (2010)), however, for purpose of testing software capabilities and data flow our simplified representation of $a*_{\phi,UV}(\lambda)$ should be sufficient.

The $a*_{\phi}(\lambda)$ spectrum over the UV-VIS-NIR spectral range is then assembled as:

$$a^*_{\phi}(<\ 400) = a^*_{\phi,UV}(\lambda <\ 400) \times a^*_{\phi,VIS}(400), (13a)$$

$$a^*_{\phi}(400 \geq \lambda \geq 700) = a^*_{\phi,VIS}(\lambda), (13b)$$

$$a^*_{\phi}(\lambda > 700) = a^*_{\phi,NIR}(\lambda > 700) \times a^*_{\phi,VIS}(700). (13c)$$

Finally, $R_{rs}(\lambda)$ is then calculated as follows (Lee et al., 2002):

$$R_{rs}(\lambda) = \frac{0.52r_{rs}(\lambda,0^-)}{1.0-1.7r_{rs}(\lambda,0^-)}. (14)$$

The input values for $a_{\phi}(443)$, $a_{dg}(443)$, and $b_{bp}(443)$, and γ in the ORM are from GIOP-derived level-3 IOP data products from VIIRS/MODIS-Aqua. The ORM generates a reliable surface

reflectance $R_{rs}(\lambda; sr^{-1})$ for the full visible spectrum (Werdell et al., 2013) however it does not directly account for inelastic scattering, or chlorophyll fluorescence.

Ocean surface reflectance:

The surface reflectance, $\rho'_{surface}(\lambda; Geom)$, is the light scattered by the air-sea interface. It has two terms: the direct sun glint reflectance and the whitecap reflectance, both of which are driven by the ocean surface windspeed. It's important to remember that the sky glint reflection was calculated through the VRT model of the Rayleigh signal. The direct glint signal, however, is calculated by the two-way attenuation of the direct solar beam that is modulated by the surface glint reflectance, $L_{GN}(\lambda)$, which is modeled using Cox and Munk (1954) wave slope statistics. The TOA direct glint reflectance is then $\pi L_{GN} T_{sol} T_{sen}/\mu_0$, where μ_0 is the cosine of the solar zenith angle, and spectral (and geometric for *T*) dependency is implied.

The whitecap irradiance reflectance at the BOA, $\rho_{wc}(\lambda)$, is based on Koepke (1984) combined with the windspeed-dependent fractional coverage model of Stramksa and Petelski (2003) and the whitecap albedo spectral-dependence in the red and near-infrared from Frouin et al. (1996). The BOA irradiance reflectance is then propagated to TOA similar to the ocean reflectance as $\rho_{wc}t_{sol}t_{sen}$, with spectral and geometric dependency implied.

Absorbing gas transmittance:

The PyTOAST simulator accounts for the main absorbing gases in the atmosphere, including ozone, water vapor, and oxygen. The water vapor and oxygen transmittance are based on the HITRAN 2020 line by line (LBL) spectroscopic dataset (Gordon et al., 2022). The LBL transmittance for different column water vapor (cwv) values is calculated assuming the US standard atmospheric profile. Instrument spectral response functions are then applied to the LBL transmittances, which are then stored in an instrument-specific LUT. During simulation, the spectral water vapor transmittance at each $Geom$, T_{wv}, are interpolated from the LUT for a given slanted water vapor (wv) concentration along the path as cwv/μ, where μ is the cosine of the path zenith angle. The oxygen transmittance is calculated similarly for different path lengths of the atmosphere given the observation geometry. The ozone transmittance is calculated from the ozone optical depth assuming Beer's law, where the optical depth is determined from the spectral ozone absorption coefficient and the ozone concentration. The ozone absorption coefficients are tabulated from (Serdyuchenko et al., 2014), and spectrally integrated with the sensor spectral response functions.

Clear sky land model

Similar to propagating the ocean surface reflectance to TOA, the land reflectance at the bottom of the atmosphere is propagated to TOA by accounting for the diffuse transmittance of the aerosols and air molecules as follows:

$$\rho'_{surface}(\lambda; Geom) = \rho_{land}(\lambda; Geom)t_{sol}(\lambda; Geom)t_{sen}(\lambda; Geom). \text{ (15)}$$

ρland is the land reflectance model. Per pixel land reflectance is determined using a land albedo climatology file containing MODIS and TROPOMI data across 14 select wavelengths (328-2314 nm). The MODIS data is a global 1km resolution climatology of the surface albedo made up of the average of 17 years of data for 2001-2017. The data observed by TROPOMI is a Surface Lambertian-equivalent reflectivity (LER) at 0.125 degree resolution created from 2018 to 2021. The combined data product has a resolution of 0.125 degrees and is extrapolated to fill in the wavelength gaps at hyperspectral resolution. Pixels with negative NDVI values were determined to be snow-covered and a static snow reflectance was assigned to those locations. The global NDVI data were obtained from the ECOSTRESS spectral library (https://speclib.jpl.nasa.gov/).
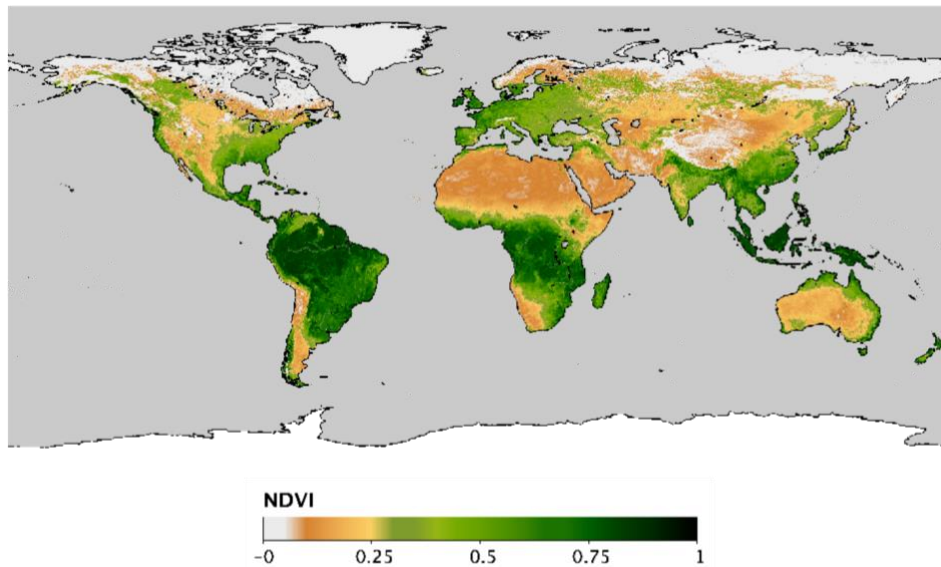

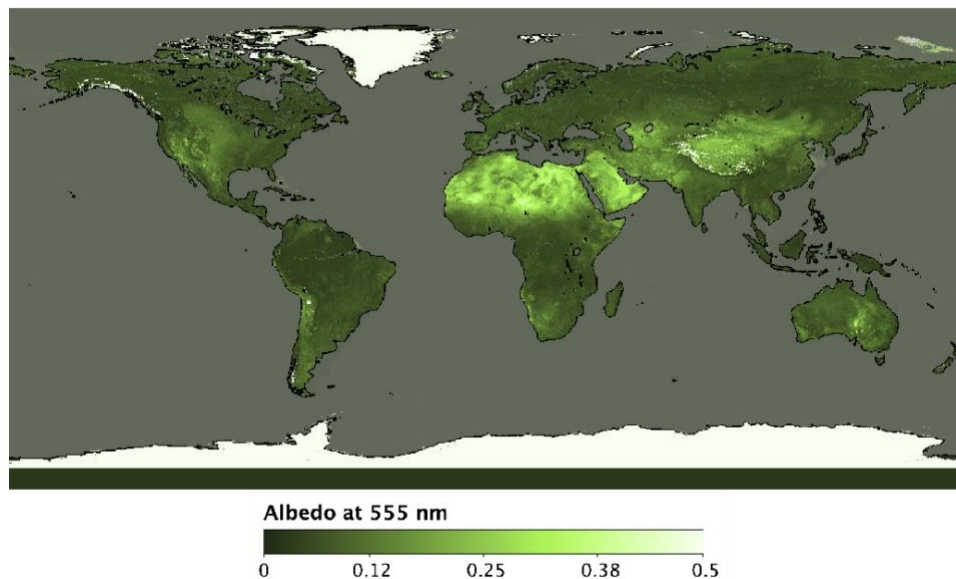Figure 1. Global map of NDVI. This data is used to define which pixels are snow-covered (negative).

Figure 2. Global land albedo map at 555 nm from MODIS. This is one of the selected bands that makes up the 14-band land reflectance climatology file that is used in the simulation.

The cloudy-sky model

Cloud coverage is defined using a VIIRS L3 mapped file (global 2km dailies) that includes cloud albedo and TOA radiance at 551nm. Pixels are first classified as either water or land, according to the standard input water mask. The cloud albedo is then used to identify where clouds exist over water. The input land albedo is similarly used to identify where clouds exist over land.

The hyperspectral OCI reflectances for cloudy pixels are created from clouds simulated with version 2.0.4 of the libRadtran radiative transfer package (freely available from http://www.libradtran.org/doku.php with the package described by Emde et al., 2016). The simulation was done with the scalar cdisort solver (16 streams per hemisphere, run in pseudospherical mode) using the in-built medium-resolution REPTRAN trace gas absorption parametrization for a US standard atmosphere (Gasteiger et al., 2014). This includes Rayleigh scattering for a surface pressure of 1 atm, and aerosols from the built-in "default" model with an optical thickness of 0.14 at 550 nm and Ångström exponent of 1 (Emde et al., 2016). Sensitivity to assumed aerosol properties within common real-world background conditions is minor. Simulations were done at REPTRAN's medium spectral resolution of 5 cm^{-1}, which translates to about 0.08 nm at 400 nm, 0.26 nm at 750 nm, and 2.6 nm at 2200 nm (somewhat finer than OCI's bandwidth in all cases). These were then convolved with OCI RSRs using numerical (trapezoid) integration and the PACE standard solar spectrum (Coddington et al., 2021).

Lookup table (LUTs) of simulated OCI spectra was created, with an angular spacing of 5, 7.5, and 20 degrees in solar zenith, viewing zenith, and relative azimuth angles, respectively. For all cases, the surface is assumed to be black (i.e. albedo of 0 at all wavelengths) and the cloud optical thickness (COT) at 550 nm is 10. There are two LUTs: one for liquid-phase clouds with a top cloud effective radius (CER) of 11 µm (and varying through the cloud following an adiabatic profile), and one for ice using the severely-roughened 8-element column aggregates model of Yang et al., (2013) with CER dependent on top altitude following van Diedenhoven et al. (2020), typically 25-40 µm (and increasing from cloud top to base by 3 µm km^{-1} above 7.5 km, and 6 µm km^{-1} below). Both types are modeled as 5 sublayers with variable CER and water content. Water content decreases and increases linearly through the clouds from top to base for liquid and ice clouds respectively. Single-scattering property data bases for these cloud types are also provided within libRadtran.

The LUTs are each generated for a set of 5 different cloud top heights (CTHs): 1, 2, 3, 4, and 5 km for liquid, and 5, 7, 9, 11, and 13 km for ice. Cloud geometric depth is taken as 50% of the vertical column for liquid clouds and 25% for ice. For the PyTOAST forward calculation, the CTH (in km) is determined as (290-BT11)/6.5 where BT11 is the VIIRS brightness temperature (BT) for band M15 (centred near 11 microns). To a first order, this approximates a cloud over a surface at 290 K with an atmospheric lapse rate of 6.5 K km^{-1}. The ice LUT is used if the resulting CTH would be

5 km or higher (i.e., BT of 257.5 K or cooler). The LUTs are interpolated linearly in PyTOAST, and VIIRS BTs which would result in CTH outside the range 1-13 km are truncated at those values.

The major limitation of the current data set is that all clouds are (fairly) opaque (COT=10) with no underlying surface. However, this offers computational simplicity of the code (no surface spectrum needs to be defined, no pixel-level COT field needs to be supplied, and with COT=10 retrieval results are in most cases likely fairly insensitive to an algorithm's assumed COT) while (through variation of CTH) offering the ability to test the implementation of the at-launch cloud top altitude retrieval algorithm (Sayer et al., 2023) with a semi-realistic distribution of heights driven by VIIRS BT. A secondary limitation is the angular resolution of the LUTs, which could more easily be improved in future simulation versions.
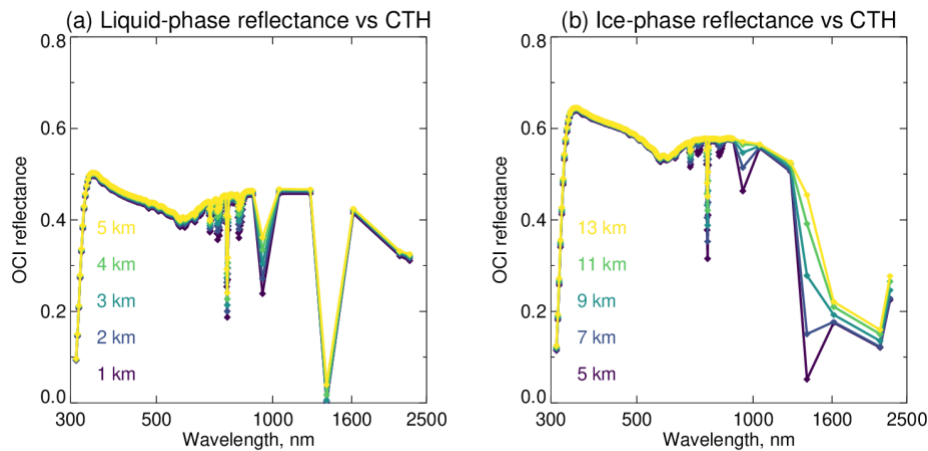

Figure 3: Simulated cloud reflectance at TOA for (a) liquid and (b) ice-phase clouds, as described in the text, as a function CTH (colours). These simulations are drawn from the cloud LUT for solar zenith, viewing zenith, and relative azimuth angles of 20, 30, and 60 degrees, respectively.

Implementation

PyTOAST flow diagram

PyTOAST relies on modeling the TOA observations based on realistic geophysical data retrieved from ocean color sensors as well as global models such as MERRA-2. The figure below shows the flow diagram of data, where the orbit geometries from OCI, metrological data from MERRA-2, and Level-3 geophysical data from MODIS, VIIRS, and OMI are used as an input to the pre-computed RT forward model LUT.
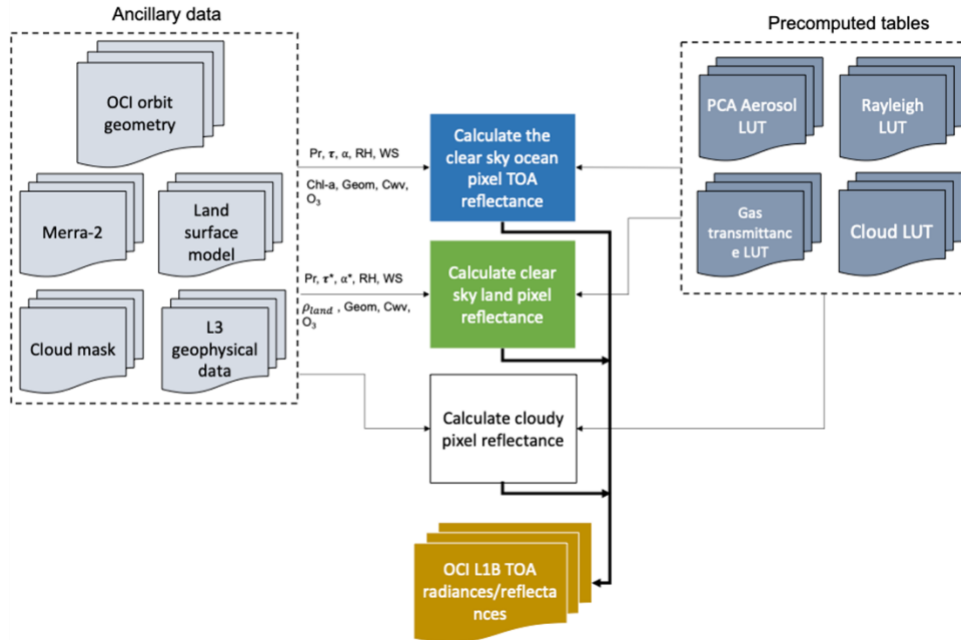
Figure 4: Flow diagram of PyTOAST

A multidimensional interpolation process of the pre-computed LUT calculates the aerosol and molecular scattering, the gas absorption of the atmosphere, and the surface radiance of land and ocean, as well as the cloud reflectance. The output TOA radiance is then stored in a standard Level 1B format NetCDF file.

Figure 5 shows an illustration of the TOA radiance, $L_t(\lambda)$, calculation for clear sky ocean pixels without clouds. The aerosol optical depth is obtained from the GMAO aerosol transport model, MERRA-2, at ~50 km spatial resolution. The aerosol radiance is calculated from the Angstrom coefficient, relative humidity, wind speed, ozone concentration, water vapor, and surface pressure, all coming from MERRA-2 at 50 km. The ORM model calculates the $R_{rs}(\lambda)$ given the Chl-a concentration and IOPs (ADG_443, APH_443, BBP_443, BBP_S) from the Level-3 32-day rolling average from MODISA. Finally, the earth-sun distance is calculated for each pixel to adjust the TOA radiance level.

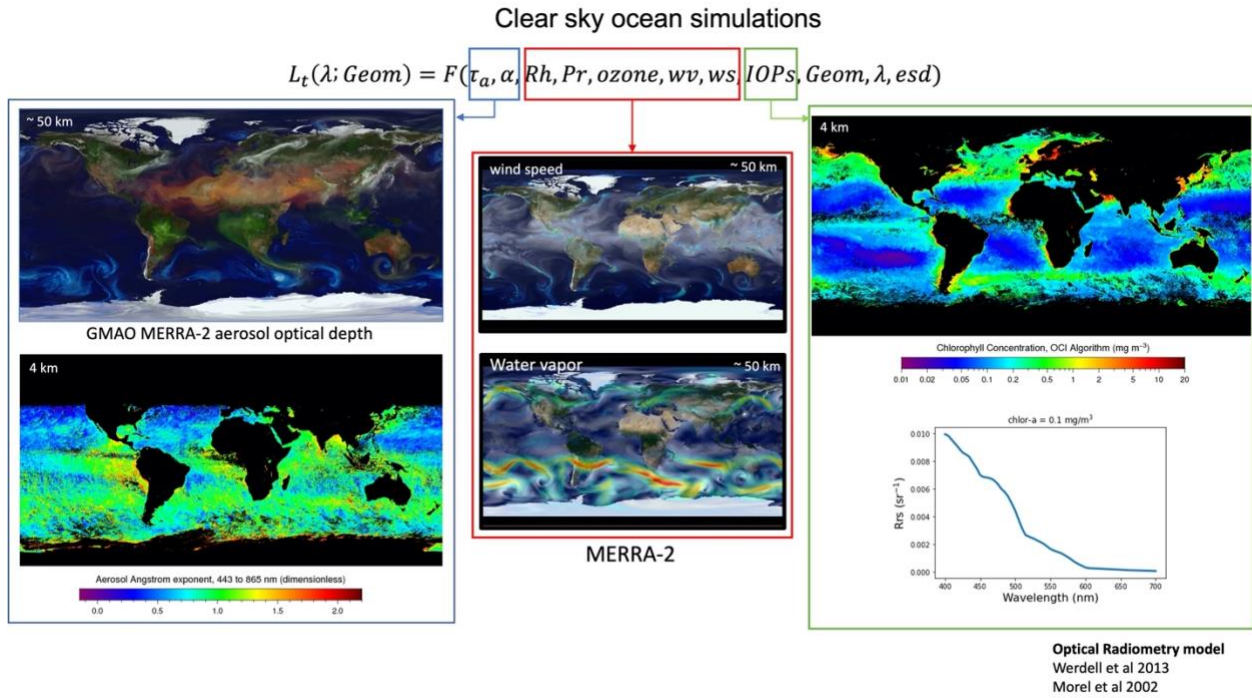Figure 5: Illustration of the TOA radiance calculation for clear sky ocean pixel.
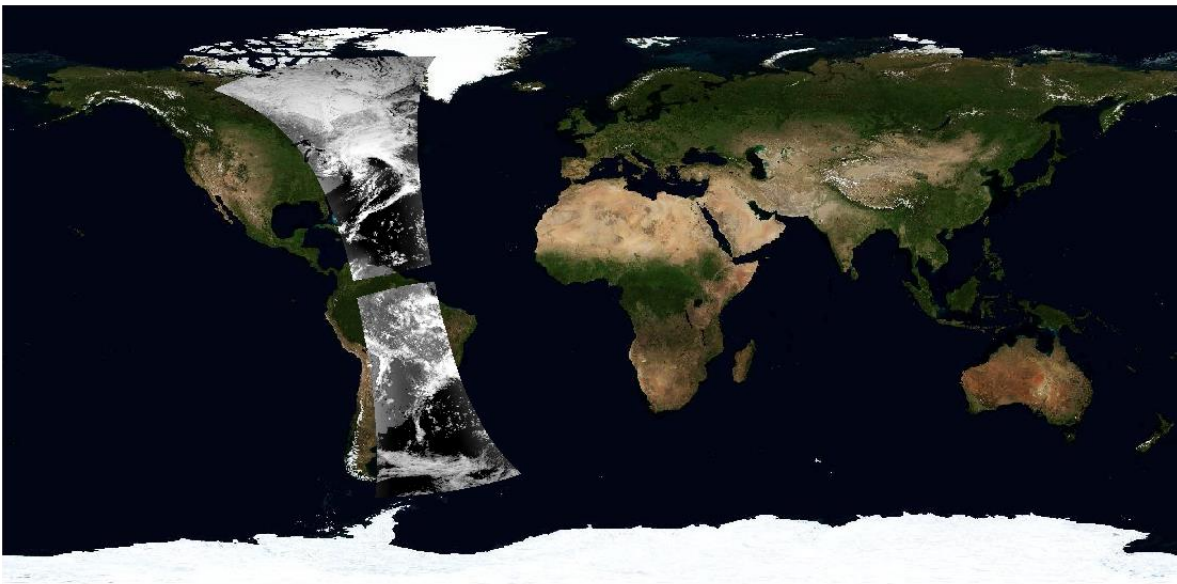

Figure 6: An orbit example demonstrating the PyTOAST simulations of the TOA radiance as observed from OCI for March, 22nd , 2019.

Cloudy pixels are located based on the VIIRS Level-3 cloud mask, where the hyperspectral TOA cloud radiance is scaled given the observed VIIRS TOA radiance at the mid-visible wavelengths.

Figure 6, shows an example of the simulated TOA radiance from PyTOAST for an OCI orbit for March 22nd 2019. The example shows the binned data for various 5-min OCI granules observed along the orbit. The simulation captures a large dynamic range of TOA radiances from ocean, land, and cloudy pixels. The gap along the tropical region is due to the tilting operation of the OCI instrument, as designed to minimize direct sun glint.

Table 1: List of Acronyms

Acronym	Definition
PyTOAST	Python Top of Atmosphere Simulation Tool
PACE	Plankton, Aerosol, Cloud, ocean Ecosystem
TOA	Top of Atmosphere
MODIS	Moderate Resolution Imaging Spectroradiometer
VIIRS	Visible Infrared Imaging Radiometer Suite
OCI	Ocean Color Instrument
LUT	Look up table
VRT	Vector Radiative Transfer
BOA	Bottom of Atmosphere
IOPs	Inherent Optical Properties
LBL	Line by Line
cwv	Column water vapor
OMI	Ozone Monitoring Instrument
UV	Ultraviolet
ECOSTRESS	ECOsystem Spaceborne Thermal Radiometer Experiment on Space Station
LibRadtran	Library for radiative transfer
cdisort	C version of Discrete Ordinates Radiative Transfer Program
REPTRAN	Gas absorption parameterization library
GMAO	Global Modeling and Assimilation Office
MERRA-2	Modern-Era Retrospective Analysis for Research and Applications, Version 2
NetCDF	Network Common Data Form
ORM	Optical Radiometry Model
VIS	Visible spectrum

Table 2: Normalized spectral absorption coefficient for phytoplankton in the UV (300 – 400 nm).

Wavelength (nm)	$a_{\phi,UV}^{*}$	Wavelength (nm)	$a_{\phi,UV}^{*}$	Wavelength (nm)	$a_{\phi,UV}^{*}$
300	8.169E-01	340	8.210E-01	380	8.300E-01
301	8.168E-01	341	8.146E-01	381	8.387E-01
302	8.165E-01	342	8.074E-01	382	8.473E-01
303	8.160E-01	343	7.994E-01	383	8.557E-01
304	8.152E-01	344	7.908E-01	384	8.639E-01
305	8.141E-01	345	7.816E-01	385	8.716E-01
306	8.129E-01	346	7.718E-01	386	8.790E-01
307	8.116E-01	347	7.617E-01	387	8.860E-01
308	8.106E-01	348	7.514E-01	388	8.927E-01
309	8.098E-01	349	7.413E-01	389	8.992E-01
310	8.093E-01	350	7.320E-01	390	9.059E-01
311	8.091E-01	351	7.238E-01	391	9.128E-01
312	8.091E-01	352	7.171E-01	392	9.202E-01
313	8.091E-01	353	7.119E-01	393	9.280E-01
314	8.091E-01	354	7.082E-01	394	9.363E-01
315	8.091E-01	355	7.057E-01	395	9.452E-01
316	8.092E-01	356	7.043E-01	396	9.546E-01
317	8.096E-01	357	7.036E-01	397	9.648E-01
318	8.105E-01	358	7.037E-01	398	9.757E-01
319	8.118E-01	359	7.043E-01	399	9.874E-01
320	8.136E-01	360	7.056E-01	400	1.000E+00
321	8.156E-01	361	7.075E-01		
322	8.177E-01	362	7.102E-01		
323	8.198E-01	363	7.137E-01		
324	8.218E-01	364	7.179E-01		
325	8.235E-01	365	7.227E-01		
326	8.252E-01	366	7.279E-01		
327	8.267E-01	367	7.334E-01		
328	8.281E-01	368	7.391E-01		
329	8.295E-01	369	7.451E-01		
330	8.309E-01	370	7.514E-01		
331	8.323E-01	371	7.579E-01		
332	8.336E-01	372	7.648E-01		
333	8.347E-01	373	7.720E-01		
334	8.354E-01	374	7.796E-01		
335	8.355E-01	375	7.875E-01		
336	8.348E-01	376	7.957E-01		
337	8.331E-01	377	8.041E-01		
338	8.303E-01	378	8.127E-01		
339	8.262E-01	379	8.213E-01		

References:

Ahmad, Z., Franz, B.A., McClain, C.R., Kwiatkowska, E.J., Werdell, J., Shettle, E.P. and Holben, B.N., 2010. New aerosol models for the retrieval of aerosol optical thickness and normalized water-leaving radiances from the SeaWiFS and MODIS sensors over coastal regions and open oceans. *Applied optics*, *49*(29), pp.5545-5560.

Anderson, S.M., Morton, J., and Mauersberger, K.. "Near-infrared absorption spectra of 16O3 and 18O3: Adiabatic energy of the 1A2 state?." The Journal of Chemical Physics 93.6 (1990): 3826-3832.

Anderson, Stuart M., Maeder, J., and Mauersberger, K. "Effect of isotopic substitution on the visible absorption spectrum of ozone." The Journal of chemical physics 94.10 (1991): 6351-6357

Bodhaine, B.A., Wood, N.B., Dutton, E.G. and Slusser, J.R., 1999. On Rayleigh optical depth calculations. *Journal of Atmospheric and Oceanic Technology*, *16*(11), pp.1854-1861.

Bricaud, A., Morel, A., Babin, M., Allali, K., Claustre, H., 1998. Variations of light absorption by suspended particles with chlorophyll a concentration in oceanic (case 1) waters: Analysis and implications for bio-optical models. J. Geophys. Res. Oceans 103, 31033–31044. https://doi.org/10.1029/98JC02712

Brion, J., Chakir, A., Charbonnier, J., Daumont, D., Parisse, C., Malicet, J., 1998. Absorption Spectra Measurements for the Ozone Molecule in the 350–830 nm Region. J. Atmospheric Chem. 30, 291–299. https://doi.org/10.1023/A:1006036924364

Coddington, O. M., Richard, E. C., Harber, D., Pilewskie, P., Woods, T. N., Chance, K., Liu, X., and Sun, K., 2021. The TSIS-1 Hybrid Solar Reference Spectrum, Geophys. Res. Lett., 48, e2020GL091709, https://doi.org/10.1029/2020GL091709

Cox, C. and Munk, W., 1954. Measurement of the roughness of the sea surface from photographs of the sun's glitter. *Josa*, *44*(11), pp.838-850.

van Diedenhoven, B., Ackerman, A. S., Fridlind, A. M., Cairns, B., & Riedi, J, 2020. Global statistics of ice microphysical and optical properties at tops of optically thick ice clouds. *Journal of Geophysical Research: Atmospheres*, 125, e2019JD031811. https://doi.org/10.1029/2019JD031811

Emde, C., R. Buras-Schnell, A. Kylling, B. Mayer, J. Gasteiger, U. Hamann, J. Kylling, B. Richter, C. Pause, T. Dowling, and L. Bugliaro, 2016. The libradtran software package for radiative transfer calculations (version 2.0.1). *Geoscientific Model Development*, 9(5):1647-1672, https://gmd.copernicus.org/articles/9/1647/2016/

Frouin, R., Schwindling, M. and Deschamps, P.Y., 1996. Spectral reflectance of sea foam in the visible and near-infrared: In situ measurements and remote sensing implications. *Journal of Geophysical Research: Oceans*, *101*(C6), pp.14361-14371.

Gasteiger, J., Emde, C., Mayer, B., Buras, R., Buehler, S. A., and Lemke, O, 2014. Representative wavelengths absorption parameterization applied to satellite channels and spectral bands, *J. Quant. Spectrosc. Ra.*, 148, 99–115, https://doi.org/10.1016/j.jqsrt.2014.06.024

Koepke, P., 1984. Effective reflectance of oceanic whitecaps. *Applied optics*, *23*(11), pp.1816-1824.

Gordon, I.E., Rothman, L.S., Hargreaves, R.J., Hashemi, R., Karlovets, E.V., Skinner, F.M., Conway, E.K., Hill, C., Kochanov, R.V., Tan, Y., Wcisło, P., Finenko, A.A., Nelson, K., Bernath, P.F., Birk, M., Boudon, V., Campargue, A., Chance, K.V., Coustenis, A., Drouin, B.J., Flaud, J. –M., Gamache, R.R., Hodges, J.T., Jacquemart, D., Mlawer, E.J., Nikitin, A.V., Perevalov, V.I., Rotger, M., Tennyson, J., Toon, G.C., Tran, H., Tyuterev, V.G., Adkins, E.M., Baker, A., Barbe, A., Canè, E., Császár, A.G., Dudaryonok, A., Egorov, O., Fleisher, A.J., Fleurbaey, H., Foltynowicz, A., Furtenbacher, T., Harrison, J.J., Hartmann, J. –M., Horneman, V. –M., Huang, X., Karman, T., Karns, J., Kassi, S., Kleiner, I., Kofman, V., Kwabia–Tchana, F., Lavrentieva, N.N., Lee, T.J., Long, D.A., Lukashevskaya, A.A., Lyulin, O.M., Makhnev, V.Yu., Matt, W., Massie, S.T., Melosso, M., Mikhailenko, S.N., Mondelain, D., Müller, H.S.P., Naumenko, O.V., Perrin, A., Polyansky, O.L., Raddaoui, E., Raston, P.L., Reed, Z.D., Rey, M., Richard, C., Tóbiás, R., Sadiek, I., Schwenke, D.W., Starikova, E., Sung, K., Tamassia, F., Tashkun, S.A., Vander Auwera, J., Vasilenko, I.A., Vigasin, A.A., Villanueva, G.L., Vispoel, B., Wagner, G., Yachmenev, A., Yurchenko, S.N., 2022. The HITRAN2020 molecular spectroscopic database. J. Quant. Spectrosc. Radiat. Transf. 277, 107949. https://doi.org/10.1016/j.jqsrt.2021.107949

Lee, Z., Carder, K.L., Arnone, R.A., 2002. Deriving inherent optical properties from water color: a multiband quasi-analytical algorithm for optically deep waters. Appl. Opt. 41, 5755–5772. https://doi.org/10.1364/AO.41.005755

Mobley, C.D., Werdell, J., Franz, B., Ahmad, Z. and Bailey, S., 2016. Atmospheric correction for satellite ocean color radiometry.

Morel, A. and Maritorena, S., 2001. Bio-optical properties of oceanic waters: A reappraisal. *Journal of Geophysical Research: Oceans*, *106*(C4), pp.7163-7180.

Pope, R.M., Fry, E.S., 1997. Absorption spectrum (380–700 nm) of pure water. II. Integrating cavity measurements. Appl. Opt. 36, 8710–8723. https://doi.org/10.1364/AO.36.008710

Rothman, L.S., Gordon, I.E., Babikov, Y., Barbe, A., Benner, D.C., Bernath, P.F., Birk, M., Bizzocchi, L., Boudon, V., Brown, L.R. and Campargue, A., 2013. The HITRAN2012 molecular spectroscopic database. *Journal of Quantitative Spectroscopy and Radiative Transfer*, *130*, pp.4-50.

Sayer, A. M., Lelli, L., Cairns, B., van Diedenhoven, B., Ibrahim, A., Knobelspiesse, K. D., Korkin, S., and Werdell, P. J., 2023. The CHROMA cloud-top pressure retrieval algorithm for the Plankton, Aerosol, Cloud, ocean Ecosystem (PACE) satellite mission, *Atmos. Meas. Tech.*, 16, 969–996, https://doi.org/10.5194/amt-16-969-2023

Serdyuchenko, A., Gorshelev, V., Weber, M., Chehade, W., Burrows, J.P., 2014. High spectral resolution ozone absorption cross-sections – Part 2: Temperature dependence. Atmospheric Meas. Tech. 7, 625–636. https://doi.org/10.5194/amt-7-625-2014

Shettle, E.P. and Fenn, R.W., 1979. *Models for the aerosols of the lower atmosphere and the effects of humidity variations on their optical properties* (Vol. 79, No. 214). Air Force Geophysics Laboratory, Air Force Systems Command, United States Air Force.

Stramska, M. and Petelski, T., 2003. Observations of oceanic whitecaps in the north polar waters of the Atlantic. *Journal of Geophysical Research: Oceans*, *108*(C3).

Thuillier, G., Hersé, M., Foujols, T., Peetermans, W., Gillotay, D., Simon, P.C. and Mandel, H., 2003. The solar spectral irradiance from 200 to 2400 nm as measured by the SOLSPEC spectrometer from the ATLAS and EURECA missions. Solar Physics, 214(1), pp.1-22.

Wang, M., 2005. A refinement for the Rayleigh radiance computation with variation of the atmospheric pressure. *International Journal of Remote Sensing*, *26*(24), pp.5651-5663.

Werdell, P.J., Franz, B.A., Bailey, S.W., Feldman, G.C., Boss, E., Brando, V.E., Dowell, M., Hirata, T., Lavender, S.J., Lee, Z., Loisel, H., Maritorena, S., Mélin, F., Moore, T.S., Smyth, T.J., Antoine, D., Devred, E., d'Andon, O.H.F., Mangin, A., 2013. Generalized ocean color inversion model for retrieving marine inherent optical properties. Appl. Opt. 52, 2019–2037. https://doi.org/10.1364/AO.52.002019

Yang, P., Bi, L., Baum, B. A., Liou, K.-N., Kattawar, G., and Mishchenko, M, 2013. Spectrally consistent scattering, absorption, and polarization properties of atmospheric ice crystals at wavelengths from 0.2 µm to 100 µm, *J. Atmos. Sci.*, 70, 330–347, https://doi.org/10.1175/JAS-D-12-039.1